Atmospheric
Chemistry
and Physics

Secondary organic aerosol formation from α-pinene, alkanes, and oil-sands-related precursors in a new oxidation flow reactor

Kun Li, John Liggio, Patrick Lee, Chong Han, Qifan Liu, and Shao-Meng Li

Air Quality Research Division, Environment and Climate Change Canada, Toronto, Ontario M3H 5T4, Canada

Correspondence: John Liggio (john.liggio@canada.ca)

Abstract. Oil-sands (OS) operations in Alberta, Canada, are a large source of secondary organic aerosol (SOA). However, the SOA formation process from OS-related precursors remains poorly understood. In this work, a newly developed oxidation flow reactor (OFR), the Environment and Climate Change Canada OFR (ECCC-OFR), was characterized and used to study the yields and composition of SOA formed from OH oxidation of α-pinene, selected alkanes, and the vapors evolved from five OS-related samples (OS ore, naphtha, tailings pond water, bitumen, and dilbit). The derived SOA yields from α-pinene and selected alkanes using the ECCC-OFR were in good agreement with those of traditional smog chamber experiments but significantly higher than those of other OFR studies under similar conditions. The results also suggest that gas-phase reactions leading to fragmentation (i.e., C–C bond cleavage) have a relatively small impact on the SOA yields in the ECCC-OFR at high photochemical ages, in contrast to other previously reported OFR results. Translating the impact of fragmentation reactions in the ECCC-OFR to ambient atmospheric conditions reduces its impact on SOA formation even further. These results highlight the importance of careful evaluation of OFR data, particularly when using such data to provide empirical factors for the fragmentation process in models. Application of the ECCC-OFR to OS-related precursor mixtures demonstrated that the SOA yields from OS ore and bitumen vapors (maximum of ~ 0.6–0.7) are significantly higher than those from the vapors from solvent use (naphtha), effluent from OS processing (tailings pond water), and from the solvent diluted bitumen (dilbit; maximum of ~ 0.2–0.3), likely due to the volatility of each precursor mixture. A comparison of the yields and elemental ratios (H/C and O/C) of the SOA from the OS-related precursors to those of linear and cyclic alkane precursors of similar carbon numbers suggests that cyclic alkanes play an important role in the SOA formation in the OS. The analysis further indicates that the majority of the SOA formed downwind of OS facilities is derived from open-pit mining operations (i.e., OS ore evaporative emissions) rather than from higher-volatility precursors from solvent use during processing and/or tailings management. The current results have implications for improving the regional modeling of SOA from OS sources, for the potential mitigation of OS precursor emissions responsible for observed SOA downwind of OS operations, and for the understanding of petrochemical- and alkane-derived SOA in general.

1 Introduction

Over the last several decades, oil production from unconventional sources has increased significantly and is expected to continue to increase into the future due to its abundant reserves, particularly in North America (Alboudwarej et al., 2006; Mohr and Evans, 2010; Owen et al., 2010). The Alberta oil sands (OS) are a large unconventional crude oil deposit, which are extracted through both open-pit mining and in situ steam-assisted techniques. Considering the scale of OS oil production, a number of environmental concerns associated with OS air emissions have arisen, including the potential for ecosystem toxicity (Kirk et al., 2014; Harner et al., 2018) and acid deposition (Jung et al., 2011; Makar et al., 2018). Recent field measurements have shown that OS mining and processing facilities are a large source of volatile organic compounds (VOCs; Simpson et al., 2010; Li et al., 2017). Such gaseous air pollutants are rapidly transformed into secondary organic aerosol (SOA), for which the OS has

been shown to be a large source (Liggio et al., 2016). Despite the large SOA formation rates observed in the OS (~ 45–$84\,\mathrm{t\,d^{-1}}$; Liggio et al., 2016), the emission sources, chemical compositions, volatilities, and SOA-forming potentials of the precursors remain unclear. Understanding the impact of SOA on the regional $PM_{2.5}$ burden, air quality and potentially regional climate requires accurate model predictions of SOA, which have been limited by the lack of data on OS source-specific SOA precursors and their SOA-forming potential (Stroud et al., 2018).

Investigating SOA-forming potentials of hydrocarbons is generally accomplished through targeted experiments of single-precursor compounds of interest to derive a yield (Odum et al., 1996; Kroll and Seinfeld, 2008). However, in the OS, SOA precursors are highly complex mixtures with volatilities spanning the range of VOCs (saturation concentration $C^* > 3 \times 10^6\,\mathrm{\mu g\,m^{-3}}$) to semi-volatile organic compounds (SVOCs; $C^* = 0.3$–$300\,\mathrm{\mu g\,m^{-3}}$; Donahue et al., 2012; Liggio et al., 2016; Tokarek et al., 2018). As a result, using a single-species approach for studying SOA formation from OS is unrepresentative. In addition, the mix of precursors (and hence chemical properties) varies by source within any given OS facility. Precursor emissions occur throughout the OS surface mining and processing production cycle, and they originate from sources including open-pit surface mines, processing plants, and tailings ponds. The organic gases evaporated from these OS sources are mainly alkanes of diverse structure (e.g., linear, branched, and cyclic; Simpson et al., 2010; Li et al., 2017), which primarily react with hydroxyl radicals (OH) in the atmosphere, as their reactions with the NO_3 radical and O_3 are very slow (Atkinson and Arey, 2003). Consequently, the mixture of vapors evolved from the above sources is ideally suited to experimental studies of their overall SOA-forming potentials and yields with oxidation flow reactors (OFRs), where ozone is often utilized as an OH radical precursor.

The development of OFRs has recently provided a complementary approach to traditional large-volume smog chambers to investigate SOA formation processes (Kang et al., 2007; Lambe et al., 2011; Bruns et al., 2015). The advantages associated with the use of OFRs include their ability to probe the SOA-forming potentials of a real-world mixture of precursors and to study SOA formation on short timescales, simulating up to several weeks of OH radical exposure (Lambe et al., 2015; Bruns et al., 2015; Palm et al., 2016). OFRs have been utilized in numerous studies to investigate the SOA-forming potentials of bulk gasoline and diesel emissions (Tkacik et al., 2014; Karjalainen et al., 2016; Jathar et al., 2017; Simonen et al., 2017), biomass burning emissions (Ortega et al., 2013; Bruns et al., 2015), ambient air at numerous locations (Ortega et al., 2016; Palm et al., 2016), and single precursors (Kang et al., 2011; Lambe et al., 2011, 2012, 2015). The results of several OFR studies have also been used to infer the presence of gas-phase fragmentation reactions (i.e., C–C bond cleavage; Jimenez et al., 2009), the

transition between functionalization (i.e., oxygen addition) and fragmentation (Lambe et al., 2012), and the corresponding impact of these processes on SOA formation yields of single precursors and complex mixtures (Lambe et al., 2012; Tkacik et al., 2014). However, results from OFR studies vary, with some single-precursor experiments noting significantly lower SOA yields from OFRs compared to smog chambers (e.g., isoprene and *m*-xylene; Lambe et al., 2011, 2015) and others indicating similar but consistently lower yields than traditional smog chamber results (e.g., α-pinene; Bruns et al., 2015; Lambe et al., 2015). Additionally, studies of vehicle exhaust mixtures in OFRs generally exhibit reduced SOA potential relative to smog chambers at similar photochemical ages (Tkacik et al., 2014; Jathar et al., 2017; Simonen et al., 2017). Similarly, the impact of fragmentation on SOA yields in OFRs has been reported to be relatively large at moderate to high OH exposures in some studies (Lambe et al., 2012, 2015) but negligible in others (Bruns et al., 2015). Although the use of OFRs has been suggested as a complementary approach to smog chambers, such disparities between OFR experiments, and between OFR and chamber results, are likely to make the interpretation of OFR SOA yields and their application to air quality modeling systems difficult. This is particularly relevant to the use of OFRs with a complex mixture of precursors.

In this study, the application of a newly developed OFR (the Environment and Climate Change Canada OFR; ECCC-OFR) to single compounds (alkanes and α-pinene) and complex precursor mixtures is described. Alkanes are the main component of OS emissions, while α-pinene is a representative biogenic precursor which likely contributes significantly to the background SOA observed in the OS region (Liggio et al., 2016). The derived SOA yields for these single compounds are compared with those of other OFRs and smog chambers, providing improved confidence in the use of OFRs for the determination of SOA yields and in the understanding of the relative importance of fragmentation processes to SOA formation. The ECCC-OFR is further used here to study the OH-initiated formation of SOA from various OS-derived complex mixtures under low-NO_x conditions. These mixtures are representative of the potential pollution from distinct stages of the OS production cycle and/or sources. This new information on the yields of SOA from these varied OS sources and other single compounds will improve the understanding of SOA formation from this large industrial sector, advance the modeling of the OS SOA formation in regional air quality models, and improve the overall understanding of alkane-derived SOA in general.

2 Methods

SOA formation was investigated using a custom-made OFR (ECCC-OFR), which is shown schematically in Supplement Fig. S1. The design of the ECCC-OFR was partially based

on recent OFRs designs (Lambe et al., 2011; Huang et al., 2017; Simonen et al., 2017), with several specific differences described further in the Supplement (Sect. 1). Briefly, the reactor is a fused quartz cylinder with a cone-shaped diffusion inlet. The length of the cylinder is 50.8 cm, with an inner diameter of 20.3 cm. The length of the cone inlet is 35.6 cm, with a full cone angle of 30°. The conical inlet is designed to minimize the establishment of jetting and recirculation in the OFR (Huang et al., 2017), which were noted for straight OFR inlets (Huang et al., 2017; Mitroo et al., 2018). There are seven openings at the output end of the ECCC-OFR; six of them (I.D. of 0.25 in; I.D. – inner diameter) are equally spaced around the perimeter to provide side flow as exhaust with a distance to the walls of 2.5 cm, intended to reduce the impact of gas and particle wall losses on sampling. A stainless steel sampling port (O.D. of 0.25 in; O.D. – outer diameter; I.D. of 0.18 in) is located in the center of the reactor, protruding 12.7 cm into the ECCC-OFR to minimize the influence of any potential turbulent eddies induced at the end of the reactor. Computational fluid dynamics (CFD) simulations and residence time distribution (RTD) measurements were conducted for this OFR, and the results indicate that only a small area is affected by recirculation and that a near laminar flow is likely achieved (Sect. S2 and Figs. S4 and S5). The volume from the inlet of the cone to the sampling port is approximately 16 L. The total flow rate for experiments is 8 L min^{-1}, resulting in a residence time of 120 s. The sampling flow rate is approximately 1.6 L min^{-1} (determined by the flow of instruments connected), with an additional flow (6.4 L min^{-1}) pushed out of the reactor through the side ports as exhaust. Four ozone-free mercury UV lamps (BHK, Inc.) used to generate the OH radical are located in four open-ended fused quartz tubes that are parallel and external to the OFR (1.5 cm). The lamps are purged by a large flow of air (~ 30 L min^{-1}) through the quartz tubes to remove the heat generated by lamps, resulting in a working temperature of approximately 25 °C, which is slightly higher than room temperature. The entire reactor is contained in an internally mirrored polycarbonate enclosure to direct all produced light towards the reactor.

OH radicals were generated by photolysis of O$_3$ ($\sim$ 12 ppm) at 254 nm followed by reaction with water vapor, a commonly used method in many OFRs (Kang et al., 2007; Lambe et al., 2012; Liu et al., 2014). Recent OFR applications and modeling studies have demonstrated the utility of 185 nm radiation in OFRs due to ease of use in the field and due to additional OH and HO$_2$ generation (Li et al., 2015; Palm et al., 2016). However, the fused quartz tubes of ECCC-OFR limit the application of such lamps due to the low transmittance of 185 nm radiation (~ 5 %), and placement of lamps on the interior of the OFR is likely to increase turbulence and wall losses within the OFR and limit overall OFR temperature control. Consequently, 254 nm radiation lamps were used. The maximum photon flux (with four lamps on) was determined based on the measured ozone

decay and OH exposure (without precursor injection) combined with a photochemical box model characterizing radical chemistry in OFRs (Oxidation Flow Reactor Exposure Estimator 3.1; Li et al., 2015; Peng et al., 2018). The input photon flux of the model was adjusted to match the measured ozone decay and OH exposure, which resulted in a maximum photon flux estimate of $\sim 1.9 \times 10^{16}$ photons cm^{-2} s^{-1}. This photon flux is similar to the PEAR (Photochemical Emission Aging flow tube Reactor) OFR (2.3×10^{16} photons cm^{-2} s^{-1}) using the same estimation method (Ihalainen et al., 2019) and about 3 times that reported for the PAM (Potential Aerosol Mass) reactor (6.4×10^{15} photons cm^{-2} s^{-1}; Lambe et al., 2017). The relative humidity was detected at the outlet (side flow) of the reactor with a humidity sensor (Vaisala) and was maintained at 37 % ± 2 % at room temperature (21 ± 1 °C) by controlling the flow of dry and wet zero air into the reactor. The OH exposure (photochemical age) inside the reactor was estimated through the decay of CO due to its reaction with OH (Li et al., 2015). The CO was introduced into the ECCC-OFR during separate experiments to characterize OH exposure offline. The CO concentration was measured with a CO analyzer (LGR CO-23r) with a high precision (0.1 ppb). A low initial concentration of CO ($\sim$ 0.5 ppm) was used to minimize the external OH reactivity introduced by CO, hence increasing the accuracy of OH exposure estimation (Li et al., 2015). The OH radical concentration was adjusted through changes in the UV light intensity by varying the voltage applied to the lamps. The OH exposure during experiments ranged from 1.2×10^{10}–2.3×10^{12} molec cm^{-3} s, which corresponds to 0.1–18 d of photochemical age, assuming a global average OH concentration of 1.5×10^6 molec cm^{-3} (Mao et al., 2009). However, the equivalent aging time is significantly shorter for urban areas and OS production regions because of their typically higher ambient OH concentrations (Hofzumahaus et al., 2009; Stone et al., 2012). For example, the OH exposure range is equivalent to 20 min–2.7 d if assuming an average OH concentration of 1×10^7 molec cm^{-3}, as has been estimated for the plumes originating from Alberta OS operations (Liggio et al., 2016).

Vapors from α-pinene, individual alkanes (n-heptane, n-decane, n-dodecane, cyclodecane, and decalin), and various OS-related samples (with the exception of the tailings pond sample) were introduced into the ECCC-OFR by a small flow of zero air (0.5–2 mL min^{-1}) passing over the headspace of the sample material, which was placed in a glass U tube and maintained at room temperature. The OS samples included freshly mined OS ore (original and unprocessed), bitumen (processed heavy oil product), naphtha (a solvent used in OS processing), diluted bitumen (dilbit: a mixture of bitumen and solvent for transport in pipelines), and tailings pond water (waste water from the mining and processing; see Sect. S3 in the Supplement for details). The tailings pond sample (~ 2 L) was placed into a 4 L glass bottle and was bubbled into the ECCC-OFR. For some samples

with high volatilities (e.g., naphtha and *n*-heptane), the gas phase was further diluted before being injected into the reactor. The total hydrocarbon (THC) concentration entering the ECCC-OFR was determined by passing the input gas stream (in offline experiments) through a Pt-based catalytic converter maintained at 400 °C and measuring the subsequently evolved CO_2 (LI-COR LI-840A) as described by Veres et al. (2010). The evolved CO_2 concentration (ppb) is converted to the total carbon concentration (ppbC; see Table 1). The conversion efficiency of this THC system was measured to be $100\% \pm 2\%$ for several hydrocarbons in the range of C_7–C_{18} (see Sect. S7 and Fig. S2) but has been shown to be equally efficient at lower carbon numbers (Veres et al., 2010). The THC concentration was measured before and after each experiment, resulting in differences of less than 5 %. In addition, the magnitude of SOA formed for repeated experiments at the same light intensity varied by less than 5 %, further indicating the stability of the precursor concentration over time. For complex OS precursor mixtures introduced into the OFR, a volatility distribution (VD) was measured by collecting the vapor-phase compounds onto desorption tubes containing Tenax (Gerstel) followed by analysis with a thermo-desorption gas chromatography–mass spectrometer (TD-GC-MS; Agilent) utilizing a method described previously (Liggio et al., 2016). The chromatogram and the derived VD of the OS-related precursors are shown in Figs. S3 and 1 and discussed in detail in Sect. S4.

Particle size distributions at the exit of the OFR were measured with a scanning mobility particle sizer (SMPS; TSI), which were used to determine SOA yields. For a subset of experiments, ammonium sulfate (AS) seed particles were generated with an atomizer, dried with a diffusion dryer, and introduced into the reactor without size selecting. The mass concentration of the AS seed particles was approximately $20\,\mu g\,m^{-3}$ for most experiments with a number-weighted mode diameter of approximately $50\,nm$ (mass-weighted mode diameter $\sim 90\,nm$). For OS ore and naphtha, additional seed concentration experiments (~ 10 and $40\,\mu g\,m^{-3}$) were also performed to investigate the impact of seed concentration on SOA formation. Particle composition was determined using a long time-of-flight aerosol mass spectrometer (LToF-AMS; Aerodyne) with a mass resolution of 6000–8000 in V mode. The mass spectra and elemental properties of the SOA were determined using the AMS analysis software Squirrel (version 1.57I) and Pika (version 1.16I). The elemental ratios (H/C and O/C) were estimated using the improved ambient method described previously (Canagaratna et al., 2015). The SOA mass concentration was calculated by multiplying the integrated volume concentration from the SMPS (after subtracting the AS volume concentration for seeded experiments) by the effective particle density. The effective density (ρ; 1.35–1.6 for different precursors) was calculated from the vacuum aerodynamic diameter (D_{va}; obtained from the AMS) and the electric mobility diameter (D_m; obtained from the SMPS) for unseeded

experiments using the equation $\rho = D_{va}/D_m$ (Lambe et al., 2015). The same density was used for seeded and unseeded experiments.

In the current study, only low-NO_x experiments were performed for all precursors, in which the reaction with HO_2 radical dominates the fate of the peroxy radical (RO_2) formed in the initial OH reaction. Such conditions are likely to represent the atmospherically relevant scenario where OS emissions have been transported significantly downwind of the OS region (and NO consumed), over boreal forest areas, where there were few NO_x sources. In addition, the low-NO_x condition is a typical oxidation pathway parameterized in regional air quality models. The formation of OS-derived SOA under high-NO_x conditions (closer to sources) is the topic of a forthcoming publication.

3 Results and discussion

3.1 Characterization of the ECCC-OFR

3.1.1 Wall losses

Previous OFR studies have indicated that the wall losses of both gaseous precursors and formed particles are potentially important factors in influencing the SOA yield results from OFRs (Lambe et al., 2011, 2015; Huang et al., 2017; Simonen et al., 2017). The particle wall losses for the ECCC-OFR were assessed by measuring size-selected (50, 100, 150, and 200 nm diameter) inorganic (AS; Huang et al., 2017) and organic (bis(2-ethylhexyl) sebacate – BES; Lambe et al., 2011; Simonen et al., 2017) aerosol number concentrations before entering and after exiting the reactor. As shown in Fig. 2, the concentration of AS aerosols after the reactor is within $\pm 3\%$ of the concentration before the reactor. For BES, the particle transmission efficiency (P_{trans}) is 92 % at 50 nm and increases to $\sim 100\%$ for 100 nm and larger particles. This indicates that inorganic and organic particle wall losses of the ECCC-OFR were very small for the flow conditions and particle size range in the experiments and hence were not considered in further SOA yield calculations. The P_{trans} of other OFRs is also shown in Fig. 2 for comparison and indicates that the current P_{trans} is similar to that of the TSAR (TUT Secondary Aerosol Reactor; Simonen et al., 2017) and PEAR (Ihalainen et al., 2019), likely due to the similarity in design (i.e., cone-shaped inlet and sampling from the centerline; see Sect. S1). Conversely, the P_{trans} of the TPOT (Toronto Photo-Oxidation Tube), PAM glass (PAM reactor with glass wall; Lambe et al., 2011), PAM metal (PAM reactor with metal wall; Karjalainen et al., 2016), and CPOT (Caltech Photooxidation Flow Tube; Huang et al., 2017) is 15 %–85 %, 20 %–60 %, 10 %–25 %, and 20 %–45 % lower, respectively, than the ECCC-OFR across a range of particle sizes. Potential causes of these discrepancies include recirculation and turbulence induced by a straight inlet and/or output
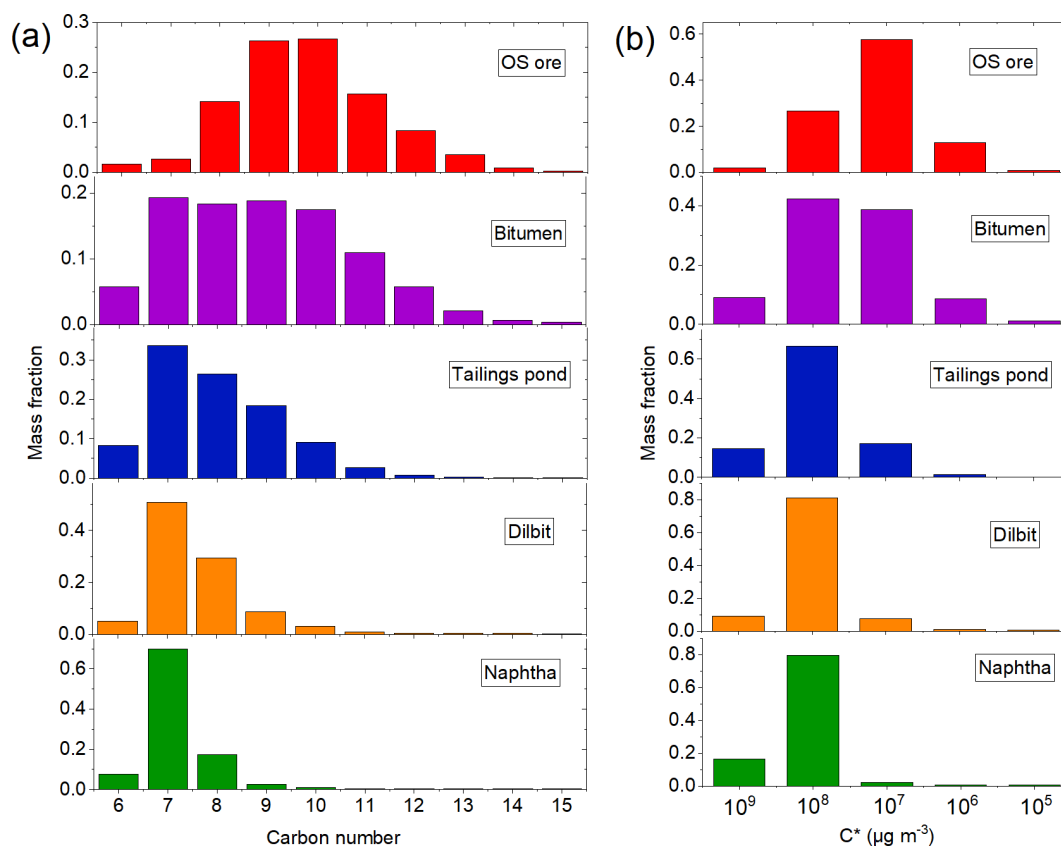
Figure 1. Volatility distribution of the OS-related precursors binned by carbon number **(a)** and effective saturation concentration C^* **(b)**.

Table 1. Initial concentrations, maximum SOA mass concentrations, and maximum yields of OS-related precursors and selected compounds.

Precursor name	Elemental formula	Initial carbon concentration (ppbC)		Maximum M_{SOA} ($\mu g\,m^{-3}$)		Maximum uncorrected yield[a]		Maximum corrected yield[a]	
		Unseeded	Seeded	Unseeded	Seeded	Unseeded	Seeded	Unseeded	Seeded
OS ore	–	137	137	35.4	46.3	0.444 (14)	0.581 (14)	0.644 (17.8)	0.708 (14)
Naphtha	–	674	677	46.7	75.1	0.118 (14.6)	0.191 (14.6)	0.193 (19.5)[b]	0.235 (14.6)
Tailing pond	–	291	288	22.7	29.8	0.134 (9.72)	0.176 (20)	0.216 (20)	0.279 (23.3)[b]
Bitumen	–	218	201	44.8	54.7	0.353 (14.5)	0.470 (11.1)	0.494 (23.2)[b]	0.545 (11.1)
Dilbit	–	710	710	41.0	69.2	0.099 (20.1)[b]	0.167 (15.1)	0.177 (20.1)[b]	0.209 (15.1)
n-Heptane	C_7H_{16}	1675	1671	43.1	85.2	0.044 (11)	0.087 (11)	0.076 (11)	0.099 (11)
n-Decane	$C_{10}H_{22}$	211.6	233.9	36.3	57.8	0.295 (11.8)	0.426 (14.6)	0.497 (16.9)[b]	0.534 (14.6)
n-Dodecane	$C_{12}H_{26}$	109.8	114.7	42.2	51.7	0.663 (9)	0.778 (9)	0.906 (21.4)[b]	0.960 (21.4)[b]
Cyclodecane	$C_{10}H_{20}$	60.3	–	56.6	–	1.639 (19)	–	2.121 (23)[b]	–
Decalin	$C_{10}H_{18}$	50.5	50.5	43.7	55.7	1.532 (23.4)[b]	1.956 (23.4)[b]	2.004 (23.4)[b]	2.298 (23.4)[b]
α-Pinene	$C_{10}H_{16}$	137	137	38.7	48.0	0.508 (11.4)	0.630 (22.3)[b]	0.731 (22.3)[b]	0.872 (22.3)[b]

[a] The number shown in the brackets is the corresponding OH exposure (10^{11} molec cm^{-3} s). [b] The SOA yield does not reach a maximum over the OH exposure range, as the highest OH exposure is shown here.

sampling end (Lambe et al., 2011), non-centerline sampling (Huang et al., 2017), and longer residence times (Huang et al., 2017) in the other OFRs (see Sect. S1), which have been noted as potential factors previously (Lambe et al., 2011; Simonen et al., 2017; Mitroo et al., 2018).

The transmission efficiencies of the ECCC-OFR for gaseous hydrocarbons (G_{trans}) in the volatile to intermediately volatile ranges were also determined using the THC conversion methodology described above to measure the concentration immediately before entering and after exiting the reactor. The G_{trans} results for three n-alkanes, specifically
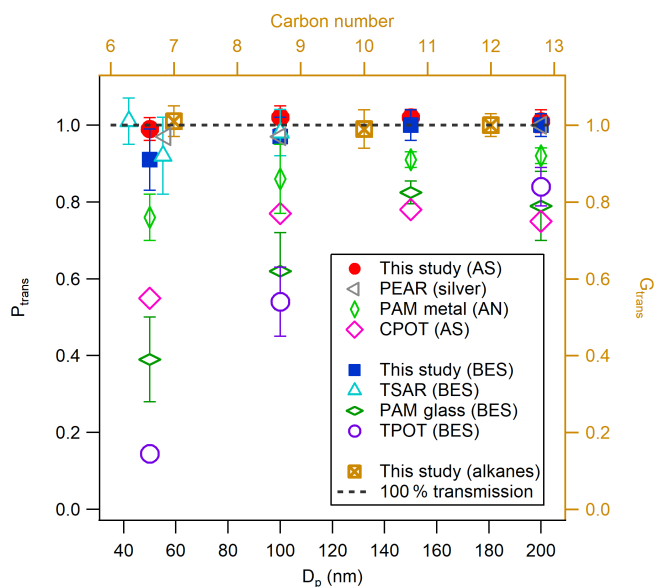
Figure 2. Particle (left and bottom axis) and gas (right and top axis) transmission efficiencies (P_{trans} and G_{trans}) for the ECCC-OFR. Particle transmission efficiencies of other OFRs are shown for comparison: PAM glass and TPOT (Lambe et al., 2011), PAM metal (Karjalainen et al., 2016), TSAR (Simonen et al., 2017), CPOT (Huang et al., 2017), and PEAR (Ihalainen et al., 2019).

n-heptane (C_7), n-decane (C_{10}), and n-dodecane (C_{12}), are shown in Fig. 2 and are approximately 100 % ± 3 %. The passivation time was 5–10 min, and the mixing ratio was 300–500 ppb for these alkanes. Measurement data with respect to hydrocarbon transmission efficiency for the other OFRs are not currently available for comparison. While the loss of hydrocarbon precursors in the ECCC-OFR may be minimal, one cannot easily measure the losses of lower-volatility oxygenated compounds directly, particularly those of intermediate products of oxidation, which largely influence measured SOA yields in smog chambers and the other OFRs (Zhang et al., 2014; Palm et al., 2016). Alternatively, we use the secondary formation of sulfuric acid to evaluate the wall losses of gas-phase products, which is described below.

The OH oxidation of SO_2 was performed in the ECCC-OFR. The SO_2 concentrations used were in the range of 24–63 ppb and the OH exposure was in the range of 3–10×10^{11} molec cm^{-3} s, which are similar to those used in a previous PAM study (Lambe et al., 2011). The yield of sulfuric acid was calculated using a method described previously (Lambe et al., 2011) and is shown in detail in Sect. S5. As shown in Fig. S6, the yield of sulfuric acid is 100 % ± 4 % in this study, which is in agreement with the expected yield (Sect. S5). The yield here is significantly higher than that obtained in previous OFR study using similar SO_2 concentrations and OH exposures (PAM and TPOT), which are mainly in the range of ∼ 15 %–50 % (Lambe et al., 2011). This may be a result of lower wall losses in the current OFR

for gas-phase sulfuric acid and/or particles. Given that sulfuric acid is not impacted by photolysis or fragmentation, the results here suggest that wall losses and interactions within the ECCC-OFR are significantly lower than previous OFRs that utilize straight inlets (PAM and TPOT).

3.1.2 SOA yields and fragmentation

An important performance characteristic of an OFR is the ability to derive SOA yields consistent with previous results in traditional chamber experiments (Bruns et al., 2015; Lambe et al., 2015). The SOA yields from the ECCC-OFR (under low-NO_x conditions) for selected individual compounds (α-pinene, n-decane (C_{10}), and n-dodecane (C_{12})), as a function of photochemical age or OH exposure and in the presence or absence of AS seed aerosol, are provided in Fig. 3. Under the operating conditions used here for α-pinene experiments, OH reaction contributes 64 %–98 % of the α-pinene gaseous loss across the entire OH exposure range and > 90 % after 3 equivalent days, with the α-pinene + O_3 reaction playing a minor role. The SOA yields (Y) in Fig. 3 are calculated using the mass concentration of organic aerosols (ΔM_O) and reacted parent hydrocarbons (ΔHC; see Sect. S5 for details), where $Y = \Delta M_O/\Delta HC$. Figure 3 also shows the yields from other recent smog chamber and OFR studies for the same individual precursors under low-NO_x conditions (see Table 2 for details; Ng et al., 2007; Eddingsaas et al., 2012; Lambe et al., 2012, 2015; Chen et al., 2013; Loza et al., 2014; Bruns et al., 2015; Han et al., 2016).

As most previous smog chamber studies are carried out at relatively low OH exposures, limited data can be used for comparison, and the majority of chamber data reside in the photochemical age of less than 3 equivalent days (3.9×10^{11} molec OH cm^{-3} s^{-1}; Table 2). However, in addition to the OH exposure level, numerous other factors may affect the SOA yield comparisons between OFR and chambers. These factors include the concentration of the gas-phase precursor utilized, the presence or absence of seed aerosol, and the mass of SOA formed during experiments (Odum et al., 1996; Donahue et al., 2006; Kroll et al., 2007; Kroll and Seinfeld, 2008; Hallquist et al., 2009). Nonetheless, the α-pinene SOA yields in the ECCC-OFR are similar to previous chamber experiments at similar OH exposures (Fig. 3a; Table 2). Given the known dependence of yield on SOA mass and precursor concentration (Odum et al., 1996; Kroll and Seinfeld, 2008), slightly higher yields for α-pinene are expected from chamber studies (and observed), as some experiments were performed at SOA mass levels and gaseous precursor concentrations 3–14 and 3–15 times (Ng et al., 2007; Eddingsaas et al., 2012; Bruns et al., 2015) greater than the current study (22–42 µg m^{-3} and 13.7 ppb; see Table 2 for details). Considering the impact of these conditions on yields, the ECCC-OFR SOA yields of α-pinene are in reasonable agreement with those derived from chamber studies. However, in the case of alkanes, the agreement is sig-
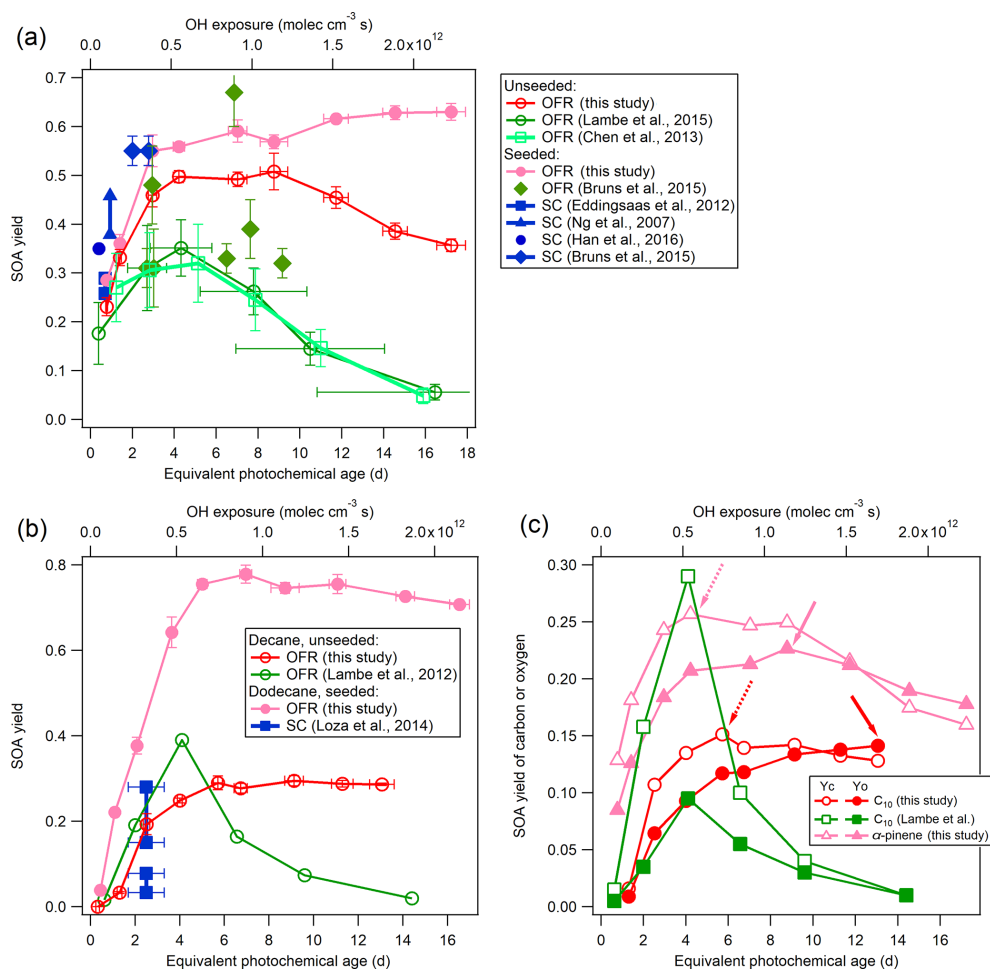
Figure 3. Low-NO_x SOA yields of α-pinene **(a)**, n-decane (C_{10}), and n-dodecane (C_{12}) **(b)** compared to previous studies using OFRs and smog chambers (SCs; Ng et al., 2007; Eddingsaas et al., 2012; Lambe et al., 2012, 2015; Chen et al., 2013; Loza et al., 2014; Bruns et al., 2015; Han et al., 2016). The details regarding these comparisons are shown in Table 2. **(c)** SOA carbon and oxygen yields (Y_C and Y_O) for single precursors for unseeded experiments in the current study and in a previous study (Lambe et al., 2012). Dashed and solid arrows indicate the maximum of Y_C and Y_O, respectively.

nificantly different. While the initial n-dodecane concentration and OA concentration (upper limit) in a previous study (Loza et al., 2014) were ~ 3 times higher than this study (Table 2), the corresponding SOA yields were significantly lower (Fig. 3b) than the current results. The known impact of gaseous wall loses on SOA yields in environmental chambers (Zhang et al., 2014) suggests that the long residence time of those particular experiments (~ 36 h; Loza et al., 2014) likely resulted in significant intermediate gaseous product wall losses and correspondingly low SOA yields compared to the ECCC-OFR (which has minimal wall losses).

While the SOA yields for single precursors from the present study are in reasonable agreement with traditional chamber data, they are significantly larger than those of other OFR data sets (Lambe et al., 2012, 2015; Chen et al., 2013; Bruns et al., 2015; Fig. 3a and b). With the exception of the lowest OH exposure data point for α-pinene ox-

idation, the SOA yields quickly diverge from each other after approximately 2 equivalent photochemical days (a factor of 4 larger in this study after ~ 10 equivalent days) for unseeded experiments, despite initial concentrations of α-pinene (41–100 ppb) and SOA mass ($90\,\mu g\,m^{-3}$) in previous OFR experiments (Chen et al., 2013; Lambe et al., 2015) being considerably higher than the current study (13.3 ppb and $37.9\,\mu g\,m^{-3}$) at similar photochemical ages (Table 2). For seeded experiments of α-pinene, the current SOA yields are higher than those reported by Bruns et al. (2015), despite their precursor concentration and SOA mass being 10–25 and 5–24 times higher than this study (13.7 ppb and $41.9\,\mu g\,m^{-3}$; Table 2). Similarly, the present SOA yields for n-decane (C_{10}) diverge from previously reported results (Lambe et al., 2012; Fig. 3b), with the present SOA yields being up to a factor of 4 higher after ~ 10 equivalent photochemical days (1.3×10^{12} molec cm^{-3} s OH exposure). It is noteworthy that

Table 2. Comparison of experimental conditions and SOA yields with previous studies.

Precursor name	M_{seed} (μg m^{-3})	Precursor (ppb)	M_{SOA} (μg m^{-3})	SOA yield	OH$_{exp}$ (10^{11} molec cm^{-3} s)	Reactor[c]	Reference
α-Pinene	0	41–100	–	0.35[a]	5.57	OFR	Lambe et al. (2015)
	0	50.6	90	0.32[a]	6.6	OFR	Chen et al. (2013)
	0	13.7	37.9	0.50[b]	5.44	OFR	This study
	13–19	44.5–47.7	63.5–76.6	0.26–0.29	0.91	SC	Eddingsaas et al. (2012)
	14–21	13.8–47.5	29.3–121.3	0.38–0.46	1.21	SC	Ng et al. (2007)
	12.6	19.6	34.1	0.35	0.52	SC	Han et al. (2016)
	21	13.7	21.8	0.29[b]	1	OFR	This study
	10–60	192–200	540–570	0.55–0.56	2.6–3.6	SC	Bruns et al. (2015)
	10–60	137–347	200–1000	0.31–0.67	3.5–11.9	OFR	Bruns et al. (2015)
	21	13.7	41.9	0.55[b]	3.9	OFR	This study
n-Decane	0	102	231	0.39[a]	5.3	OFR	Lambe et al. (2012)
	0	23.4	30.4	0.25[b]	5.2	OFR	This study
n-Dodecane	17–24	8.2–34	1.8–65	0.03–0.28	3.24	SC	Loza et al. (2014)
	21	9.6	24.3	0.37[b]	2.72	OFR	This study

[a] Maximum SOA yield. [b] The SOA yield at the OH exposure similar to above studies. [c] OFR: oxidation flow reactor. SC: smog chamber.

the yields for n-decane from the present study and reported by Lambe et al. (2012) are in reasonable agreement for up to 2 equivalent days (2.6×10^{11} molec cm^{-3} s OH exposure). However, this is likely fortuitous, as the SOA mass concentration and precursor concentration in the study by Lambe et al. (2012; 231 μg m^{-3} and 102 ppb) was an order of magnitude higher than in the present study (30.4 μg m^{-3} and 23.4 ppb; Table 2), which will enhance the gas–particle partitioning process and lead to higher yields. Such an effect has been observed in C$_{15}$ SOA experiments (Lambe et al., 2012), where decreasing the aerosol mass concentration from 100 to 16 μg m^{-3} reduced the SOA yield from 0.69 to 0.21.

The decrease in yield at longer photochemical ages (higher OH exposures) in previous OFR studies (Fig. 3a and b) has been attributed to gas-phase fragmentation leading to higher-volatility SOA products, with a transition point between functionalization and fragmentation being observed at the maximum carbon yield (Lambe et al., 2012). The SOA carbon and oxygen yields (Y_C and Y_O) for α-pinene and n-decane from the current experiments are shown in Fig. 3c following the approach outlined elsewhere (Kroll et al., 2009; Lambe et al., 2012) and presented in detail in the Supplement (Sect. S5). In the absence of gaseous wall losses, the impact of fragmentation may be indicated by a relatively larger decrease in Y_C at higher OH exposure compared to Y_O (Kroll et al., 2009; Lambe et al., 2012). Such an effect is observed in the present results for both α-pinene and n-decane (Fig. 3c), with Y_C decreasing by 38 % and 15 % over 7 and 13 photochemical days, respectively. The maximum Y_O is at a higher photochemical age compared to Y_C for SOA formed from both precursors ($\sim$ 9 and 4 photochemical days for α-pinene;

$\sim$ 13 and 6 photochemical days for n-decane), further consistent with a transition from functionalization to fragmentation in these experiments, as indicated in Fig. 3c. However, the relative impact of fragmentation on the overall SOA yields here is in contrast to that suggested previously (Lambe et al., 2012; Fig. 3a and b). The maximum Y_C for n-decane here is observed at a higher photochemical age of 6 d, compared to 4 d seen by Lambe et al. (2012), and the decrease in Y_C and overall Y is also significantly less (15 % vs. $\sim$ 95 % for Y_C; < 5 % vs. $\sim$ 95 % for Y).

Given the similarity in the OH exposure range used between studies, and the generally higher SOA mass concentration (and precursor concentration) in previous OFR studies (Lambe et al., 2012, 2015; Chen et al., 2013), the present results suggest that gaseous wall losses during the oxidation process may have reduced previously observed yields in their OFRs, thereby leading to an overemphasis on the importance of fragmentation in SOA formation. It is notable that the relative impact of fragmentation here, although small, may also not be fully applicable to the ambient atmosphere due to the fate of low-volatility organic compounds (LVOCs) in the OFRs. Accounting for the fate of LVOCs reduces the potential importance of fragmentation to SOA formation in this study and the ambient atmosphere even further, as is described below (Sect. 3.1.3).

3.1.3 Fate of LVOCs

Previous studies have demonstrated that SOA yields derived in OFRs at high OH exposures (and other conditions) have likely been underestimated due to differences between the fates of LVOCs in OFRs and the ambient atmosphere (Palm

et al., 2016). There are four possible fates associated with LVOCs in an OFR: condensation to aerosol, reaction with OH, condensation to the OFR walls, and exiting the OFR (then lost on sampling walls). However, in the ambient atmosphere, condensation to aerosol is the dominant fate of LVOCs, indicating that the other three possible fates are limitations of the OFR (Palm et al., 2016). To characterize the ECCC-OFR with respect to the fate of LVOC and improve the subsequent applicability of the data to the ambient atmosphere, we modeled the fate of LVOCs under conditions specific to these experiments, following the approach of Palm et al. (2016), as described further in the Supplement (Sect. S6).

The modeled fates of LVOCs in the ECCC-OFR for unseeded and AS-seeded conditions are shown in Fig. 4a and b, using the parameters (OH concentration and aerosol size distribution) from α-pinene experiments. Figure 4a indicates that condensation on aerosol surfaces (in the absence of seed particles, for α-pinene-derived SOA) accounts for 70 %–80 % of the LVOC fate between $\sim$ 1–6 photochemical days, decreasing to 40 %–50 % at 16 photochemical days. These fractions are similar to an ambient OFR study conducted in Los Angeles ($\sim$ 40 %–80 %; Ortega et al., 2016) but higher than the fraction obtained at a forested site ($\sim$ 10 %–70 %; Palm et al., 2016). OH oxidation accounts for 5 %–50 % of the LVOC loss in the ECCC-OFR, increasing in importance at higher photochemical age, while LVOC wall losses and OFR-exiting fates are very small, generally at less than 5 %. For experiments using $20\,\mu g\,m^{-3}$ of AS seed particles, the fraction that condenses onto aerosol ($\sim$ 70 %–95 %; Fig. 4b) is significantly higher than that for unseeded experiments due to the presence of a higher condensational sink.

The fraction of LVOCs that condenses on aerosol ($F_{aerosol}$) for single precursors (α-pinene, n-decane, and n-dodecane) and various OS-related precursor mixtures (their yields will be discussed in the following section) is shown in Fig. 4c and d. The $F_{aerosol}$ are very similar to each other in the presence of AS seed particles regardless of the precursor, accounting for $\sim$ 95 % of the LVOC fate at less than 1 photochemical day and $\sim$ 70 % at $\sim$ 16 photochemical days. Conversely, the range of $F_{aerosol}$ is much wider for unseeded experiments (Fig. 4c and d), from $\sim$ 40 % to 80 %. The results suggest that the OFR experiments under the seeded conditions here are the most relevant to the ambient atmosphere, particularly at less than 4 photochemical days, with yields potentially requiring a relatively small upwards adjustment ($\sim$ 30 %) even at > 14 photochemical days. The model also suggests that the impact of fragmentation reactions on SOA yields (derived from this OFR), when translated to the atmosphere, is likely to be very small, as the OH reactions of LVOC never dominate the overall fate (Fig. 4b).

Given the results of Fig. 4, future OFR studies investigating SOA yields should be conducted in the presence of pre-existing seed particles to reduce uncertainties, as theoretically suggested previously (Palm et al., 2016). The estimated fate of LVOCs for seeded experiments here is used

to apply an upwards correction to α-pinene (Fig. S8) and OS-derived SOA yields (discussed in Sect. 3.2) assuming an LVOCs fraction of 80 % in SOA (see Sect. S6 for details). As OH concentrations in smog chambers are generally much lower than studies with the OFRs, the LVOCs in smog chamber will mostly condense on aerosols, which is similar to the real atmosphere. Hence, when comparing the OFR yields to smog chambers, an LVOC-fate correction should be applied. As shown in Fig. S8, the SOA yields from α-pinene in the current OFR after correction are in good agreement with previous smog chamber results despite the lower SOA mass concentration and precursor concentration.

3.2 SOA yields of OS-related precursors

The ECCC-OFR was used to investigate the SOA yields of complex precursor mixtures, specifically those derived from OS sources (see Methods). The SOA yields of these OS-related precursor mixtures are shown in Fig. 5a for unseeded experiments performed in an atmospherically relevant SOA mass concentration range ($< 50\,\mu g\,m^{-3}$; Table 1). The SOA yield in this case is defined similarly to that in Sect. 3.1.2 but accounts for the calculated H/C ratio (Table S1) and measured carbon number distribution of emissions (Fig. 1a), as described in detail in Sect. S5. Briefly, the H/C ratios of precursors were used to calculate the initial precursor mass concentrations from the measured total carbon concentration. The reacted mass concentrations were calculated using the rate constant with OH of corresponding n-alkanes that have the same carbon number as the average value of carbon number distributions. As demonstrated in Fig. 5a, the freshly mined OS ore results in the highest yields among the five precursor mixtures, with a maximum of 0.44 ± 0.05 at approximately 11 atmospheric equivalent photochemical days (1.4×10^{12} molec cm^{-3} s OH exposure, corresponding to approximately 1.6 d in OS plumes; Liggio et al., 2016), followed by processed bitumen, with slightly lower yields over the entire range of photochemical age (with a maximum of 0.35 ± 0.03). The SOA yields of naphtha, dilbit, and tailings pond emissions are significantly lower, with maximum SOA yields of approximately 0.1 ± 0.01 to 0.13 ± 0.01. The difference in yields between source mixtures (Fig. 5a) can be qualitatively explained by the volatility distributions (VDs) of these precursors (Fig. 1), with precursors of lower volatility (higher carbon number) having higher SOA yields (Lim and Ziemann, 2005, 2009). In this case, naphtha solvent and OS ore emissions represent volatility endpoints (high and low, respectively), with other precursor mixtures being derived from a combination of these (see Sect. S4 for details). Although these precursors have very different SOA yields, their AMS mass spectra (Fig. S9) are similar, indicating a similar main precursor composition (alkanes).

SOA yields from several straight chain pure compounds (C_7, C_{10}, and C_{12}) were also investigated in the ECCC-OFR to provide additional information on the nature of the OS-
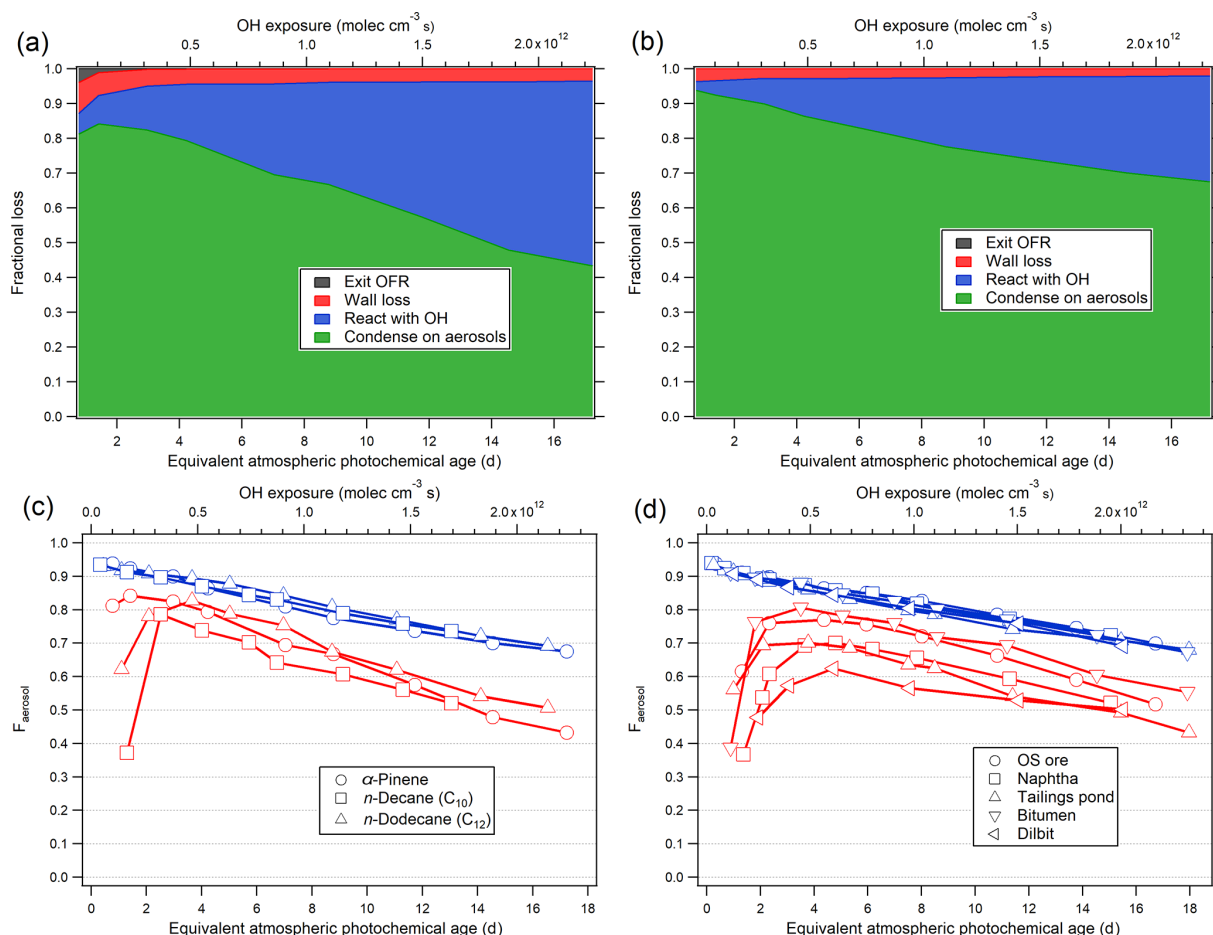
Figure 4. (a, b) The modeled fate of LVOCs in the current OFR as a function of photochemical age, for α-pinene oxidation, in the absence **(a)** and presence **(b)** of AS seed particles. **(c, d)** Fraction of LVOCs that condense on aerosol ($F_{aerosol}$) in the OFR during the oxidation of the single precursors **(c)** and various OS-related precursors **(d)** (blue: seeded experiments; red: unseeded experiments).

related precursor mixtures and are depicted in Fig. 5a. These single compounds were selected for comparison based on the VD of the OS precursors (Fig. 1a), where heptane (C_7) represents the maximum of the VD of naphtha and dilbit, decane (C_{10}) the approximate average volatility of OS ore (see Sect. S4), and dodecane (C_{12}) a compound representative of the lower end of the VD of OS ore and processed bitumen. As shown in Fig. 5a, despite naphtha and dilbit vapors being dominated by compounds with an equivalent volatility to heptane (Fig. 1a), their SOA yields (0.11 ± 0.01) are significantly higher than the yield of heptane (0.044 ± 0.006). Similarly, OS ore emissions result in higher yields than decane, despite a comparable volatility but lower yields than C_{12}. This suggests that alkanes with a higher carbon number (and hence lower volatility and higher yield) contribute disproportionately to the overall SOA yields relative to their proportions in the precursor emissions (Fig. 1a). Alternatively, cyclic hydrocarbons in the OS-related precursors could also contribute significantly to the overall yields, as experiments for cyclodecane and decalin (a bicyclic C_{10} alkane; Fig. 5a)

result in much higher yields than decane. This is consistent with previous studies that demonstrated that cyclic alkanes have much higher yields than n-alkanes in general (Lim and Ziemann, 2009; Tkacik et al., 2012; Hunter et al., 2014). While the yields for single species alone cannot be used to distinguish between the contributions of cyclic and acyclic compounds to the observed OS-derived SOA, elemental ratios of the SOA suggest that cyclic species may be an important contributor (see Sect. 3.3).

The SOA carbon and oxygen yields (Y_C and Y_O) for the least and most volatile precursor mixtures (OS ore and naphtha solvent, respectively) are shown in Fig. 5b as an indicator of the impact of fragmentation on the derived SOA yields. Both Y_C and Y_O for OS ore and naphtha reach a maximum at approximately 11 equivalent photochemical days and then decrease with increasing photochemical age. The decrease in Y_O for OS ore and naphtha is $\sim 1\%$ per equivalent day from 11 to ~ 15–17 d. However, the Y_C values for OS ore and naphtha decrease by $\sim 2\%$–4% per day, which is higher than the decrease in Y_O. This suggests that fragmentation re-
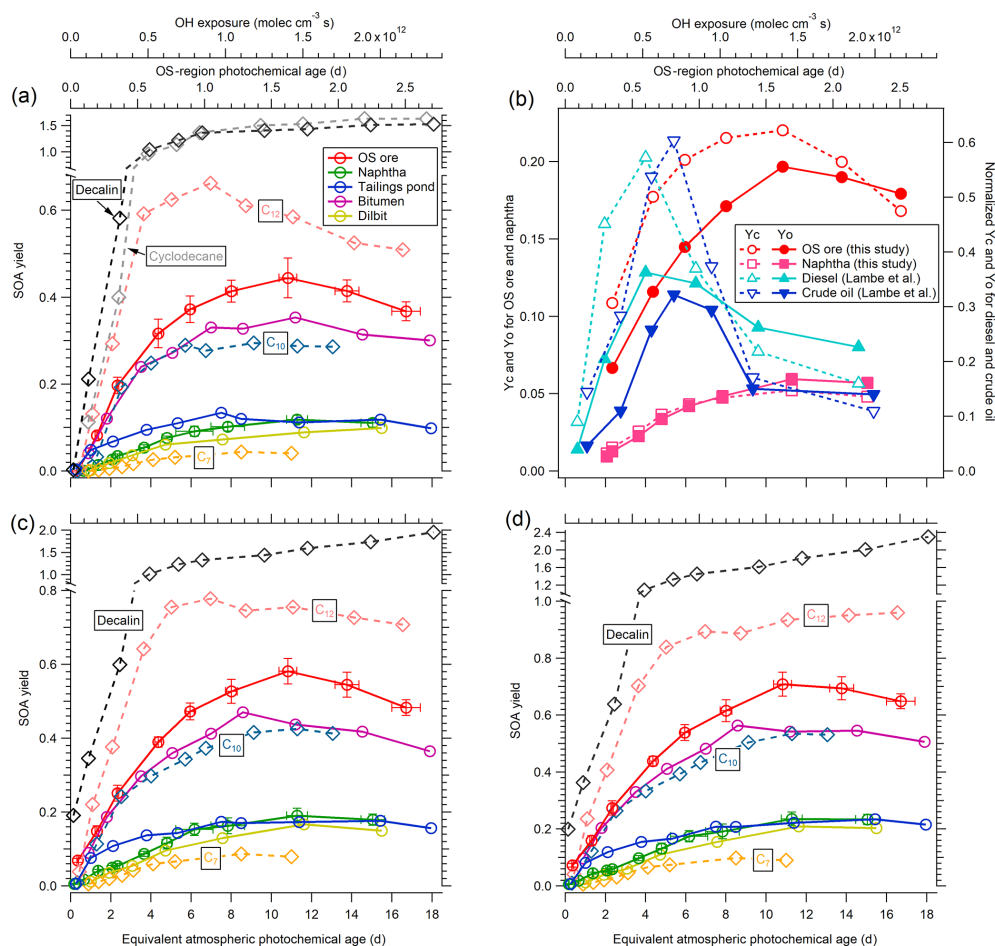
Figure 5. (a) SOA yields of OS-related precursors (OS ore, naphtha, tailings pond water, bitumen, and dilbit) for unseeded experiments as a function of equivalent photochemical age and OH exposure. SOA yields of C_7, C_{10}, and C_{12} n-alkanes; cyclodecane; and decalin are also shown for comparison. Representative error bars indicate $\pm 1\sigma$ uncertainty in measurements. **(b)** SOA carbon and oxygen yields (Y_C and Y_O) for the OS precursors of lowest and highest volatility (OS ore and naphtha solvent) compared to normalized Y_C and Y_O for diesel and crude oil (Lambe et al., 2012). **(c)** SOA yields as in **(a)** in the presence of ammonium sulfate seed particles. **(d)** LVOC-fate-corrected SOA yields of OS-related precursors and alkanes for seeded experiments. Note that the y axis ranges are different in **(a)**, **(c)**, and **(d)**.

actions increasingly influence SOA yields at higher photochemical ages for OS-related precursors, although a significant relationship between the degree of fragmentation and carbon number cannot be determined. Regardless, the overall impact of the competition between functionalization and fragmentation on the SOA yields here is small across all OS-derived precursors. This is in contrast to other types of fuel products, specifically diesel and southern Louisiana crude oil (Fig. 5b), which were shown to have SOA yields that are highly affected by fragmentation reactions (Lambe et al., 2012), although those studies were likely impacted by wall losses.

The results of experiments conducted using $20\,\mu g\,m^{-3}$ solid AS seed particles are shown in Fig. 5c. Experiments with 10 and $40\,\mu g\,m^{-3}$ AS seed particles were also performed for OS ore and naphtha but exhibited no SOA yield dependence on seed concentration (not shown), with the

same SOA yields derived in all cases. Generally, the SOA yields for all precursors are enhanced significantly in the presence of AS seed particles, with maximum yields of 0.58 ± 0.03 and 0.18 ± 0.02 for the least and most volatile OS precursors. This effect is more clearly depicted as a yield enhancement ratio ($Y_{\text{seeded}}/Y_{\text{unseeded}}$) in Fig. 6. Based on Fig. 6, it is evident that SOA from precursors with higher volatilities is more impacted by the presence of AS seed particles; SOA yield enhancement ratios for naphtha and dilbit ($\sim 60\,\%$) are higher than OS ore and bitumen ($\sim 30\,\%$) after approximately 2 equivalent photochemical days, with the ratio of tailings pond SOA being between them. It is also evident that the enhancement factor is somewhat larger during the initial stages of oxidation (up to $> 100\,\%$ at < 2 equivalent photochemical days). This is likely a result of the different LVOC fates for seeded and unseeded experiments. As shown in Sect. 3.1.3 and Fig. 4d, the fraction of LVOCs that condenses
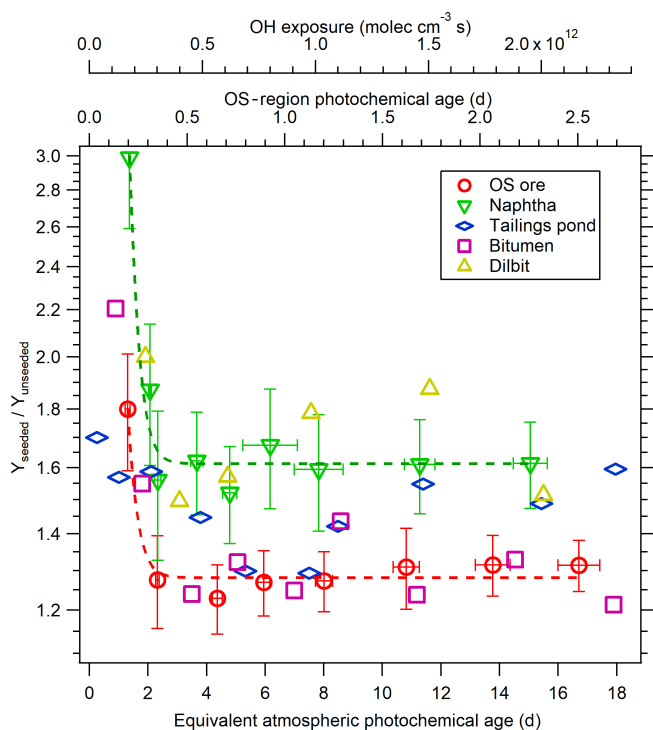
Figure 6. Yield enhancement factor due to seed particles for OS-related precursors. Dashed lines are exponential fittings for naphtha and OS ore data; error bars indicate $\pm 1\sigma$ uncertainty in measurements.

on aerosol ($F_{aerosol}$) at < 2 equivalent photochemical days for unseeded experiments is much lower than that for seeded experiments, which will lead to a larger yield enhancement ratio in the presence of seed particles. The finding that the presence of seeds can enhance the SOA yields is in agreement with various previous work (Kroll et al., 2007; Hildebrandt et al., 2009; Zhang et al., 2014; Lambe et al., 2015; Li et al., 2018). In addition to the difference in the LVOC fate discussed above, the enhanced SOA yield in the presence of seed particles can also be due to increased aerosol surface area that competes with other sinks (e.g., vapor wall losses for smog chambers) and enhances the gas–particle partitioning of semi-volatile and intermediate-volatility organic compounds (S/IVOCs), as suggested previously (Hildebrandt et al., 2009; Zhang et al., 2014; Li et al., 2018).

The OS precursor SOA yields for seeded experiments are adjusted upwards to account for the fate of formed LVOCs through normalization by the $F_{aerosol}$ above (Sect. 3.1.3), with the results of this correction being shown in Fig. 5d. Here, we assume that 80% of the SOA is LVOCs, while the other 20% is S/IVOCs (see Sect. S6 for details). Relative to the yields of Fig. 5c, the LVOC-fate-adjusted SOA yields of Fig. 5d are $\sim 4\%$ to 37% larger for all precursors, depending on the OH exposure. As noted above, the fate of LVOC in seeded experiments is primarily condensation to the aerosols, requiring a relatively small adjustment. As a

result, the seeded experiment data in Fig. 5d represent our best estimate of the SOA yields for the precursors, applicable to the ambient atmosphere (under these conditions). In this case, the maximum SOA yield for the least and most volatile precursor mixtures (OS ore and naphtha) increased from 0.58 ± 0.03 to 0.71 ± 0.04 and 0.18 ± 0.02 to 0.23 ± 0.02, respectively, after adjustment (Fig. 5d). In addition, applying an LVOC-fate adjustment results in SOA yields for most OS precursors, α-pinene, and n-alkanes generally increasing with increasing OH exposure (Figs. S8 and 5d). This further suggests, as noted above, that the fragmentation reactions will not significantly decrease the SOA yields for these species in the ambient atmosphere even after 16 equivalent photochemical days. However, uncertainties still remain when using OFRs to simulate the SOA formation processes in the real atmosphere, likely from differing fates of intermediate radicals (e.g., RO$_2$), especially at high OH exposure, as suggested very recently (Peng et al., 2019).

3.3 Elemental ratios of OS-related SOA

The elemental H/C and O/C ratios of SOA particles are illustrated in a Van Krevelen diagram (Heald et al., 2010) in Fig. 7. Figure 7 indicates that the elemental ratios of SOA from OS ore and bitumen (and its photochemical evolution) are very similar (O/C: 0.45–0.8, H/C: 1.4–1.6), as are the elemental ratios of SOA formed from naphtha, dilbit, and tailings pond water (O/C: 0.6–0.9, H/C: 1.5–1.7). This is analogous to the similarity in the yields between the same precursors as discussed above (Fig. 5) and consistent with the volatility of the precursors (Fig. 1). The lower O/C ratios of OS ore and bitumen SOA are probably due to their larger molecular size, with higher-carbon-number (i.e., lower volatility) precursors requiring less oxygen (hence fewer oxidation steps) to partition into the particle phase (Tkacik et al., 2012). The H/C ratios are also lower for SOA formed from lower-volatility precursor mixtures, which is likely a result of different H/C of the precursors, with generally lower H/C for higher-carbon-number hydrocarbons. Assuming a linear relationship in Fig. 7, the y intercept is indicative of the average H/C of the precursor mixture (Fig. S10). The intercept of naphtha and dilbit SOA (~ 2.1) is higher than OS ore and bitumen SOA (~ 1.8), indicating a higher H/C ratio for those precursors.

Similar inferences are made when comparing the evolution of the elemental ratios of SOA from various single alkane species in Van Krevelen space to that of OS precursors (Fig. 7). For example, SOA from parent n-alkanes with a successively higher carbon number (and lower volatility) move towards the bottom left of the Van Krevelen diagram. However, the position of OS-related SOA in Van Krevelen space is not consistent with the corresponding n-alkanes; naphtha, dilbit, and tailings SOA reside below n-heptane (C$_7$), despite having a very similar volatility (Fig. 1a). Similarly, OS ore and bitumen reside below n-dodecane (C$_{12}$), despite
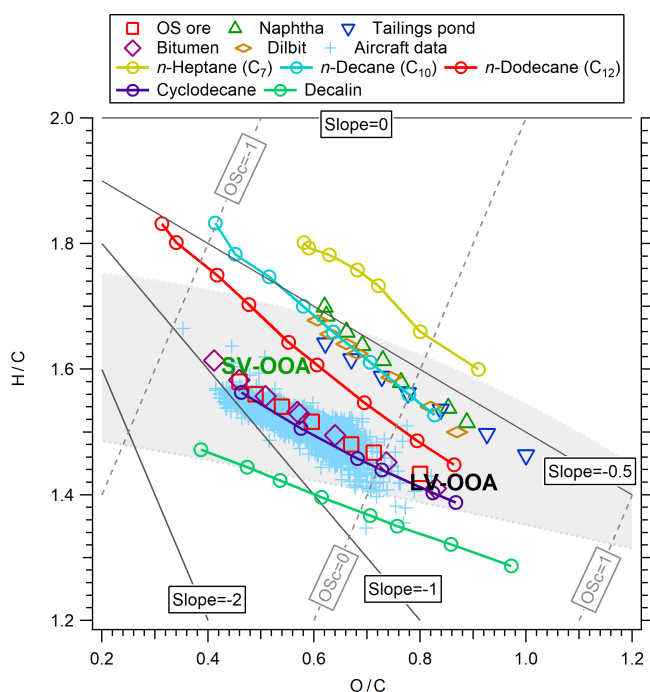
Figure 7. Van Krevelen diagram for the SOA formed from OS-related precursors, selected alkanes, and recent aircraft data in OS plumes (Liggio et al., 2016). The shaded area represents the elemental ratio space associated with ambient OOA (Ng et al., 2011).

C_{12} volatility compounds contributing little to the overall volatility distribution of precursors (Fig. 1a). This discrepancy may be explained by the contribution of cyclic alkanes, since SOA formed from cyclic structures tends to reside below acyclic alkane SOA in Van Krevelen space and near that of OS-derived SOA (e.g., cyclodecane and decalin relative to decane SOA and OS ore SOA in Fig. 7). Recent aircraft measurement indicated that the cycloalkanes contribute 13 %–27 % of the total alkanes (Li et al., 2017) for Suncor and CNRL facilities (where the OS samples were collected), which will contribute a large proportion of SOA after considering their high SOA yields (Fig. 5a, c, and d). A lower H/C ratio for SOA derived from cyclic alkanes is consistent with the parent hydrocarbon having lower H/C. The linear regression results of H/C vs. O/C for alkane precursors are listed in Table S1, from which the relationship between precursor H/C and intercept is obtained (see Sect. S5 for details). A comparison between the H/C ratios of alkanes and OS precursors demonstrates that the H/C ratios of the OS precursors are generally lower than that of the corresponding n-alkane (e.g., ~ 2.2 for naphtha and dilbit, ~ 2.3 for C_7; ~ 2 for OS ore, and ~ 2.2 for C_{10}), which is likely from the contribution of cyclic alkanes. Aromatics may also play a role in the decrease of H/C ratio of precursors; however, their contributions are likely small, according to recent aircraft measurement by Li et al. (2017; e.g., 3.7 % aromatics compared to alkanes for CNRL). In addition, the presence of aromatics

will not decrease the observed H/C and O/C of SOA; for example, the H/C and O/C of toluene SOA (1.67 and 0.85; Canagaratna et al., 2015) is similar to that of heptane SOA observed here. While the current data cannot quantitatively apportion OS precursors to various structures (cyclic vs. n-alkane or branched), the above Van Krevelen analysis suggests that cyclic compounds are an important contributor to the observed SOA.

The locations of two broad types of SOA, SV-OOA and LV-OOA (semi-volatile and low-volatility oxidized organic aerosol), from various studies (Ng et al., 2011; Canagaratna et al., 2015) and the location of the SOA downwind of the oil sands from previous aircraft measurements (Liggio et al., 2016) in Van Krevelen space are also shown in Fig. 7. The positions of SOA formed from OS-related precursors in the ECCC-OFR are generally in the range of previous ambient OOA. They are in good agreement with SV-OOA and LV-OOA for experiments simulating ~ 2 photochemical days ($\sim 2.6 \times 10^{11}$ molec cm^{-3} s OH exposure) and ~ 2 weeks ($\sim 2 \times 10^{12}$ molec cm^{-3} s OH exposure), respectively. Furthermore, SOA derived from OS ore and bitumen is more similar to ambient SV-OOA and LV-OOA than naphtha-, dilbit-, and tailings-pond-water-derived SOA (Fig. 7). This highlights the contribution of intermediate-volatility alkanes to ambient SOA in the oil sands, particularly since the SOA formed from OS ore and bitumen is in good agreement with the aircraft data (Liggio et al., 2016; Fig. 7). Hence, these results indicate that low-volatility precursors from open-pit mining sources (i.e., OS ore) are likely the largest contributors to the SOA formed downwind of the Alberta OS region, while precursors of high volatility play a minor role, likely due to their lower SOA yields.

4 Conclusions and implications

In this study, a newly designed oxidation flow reactor (ECCC-OFR) was applied to the investigation of SOA formation from single-precursor compounds (α-pinene, n-alkanes, and cyclic alkanes) and complex mixtures (OS-related precursors). The SOA yields for α-pinene and alkanes obtained in the ECCC-OFR are similar to previous smog chamber studies but significantly higher than other OFRs. The current results provide SOA yield information for alkane precursors for which limited data are available, especially at moderate to high photochemical ages (Tkacik et al., 2012; Lambe et al., 2012). In addition, the differences in yields between the current and other OFRs suggest that while OFRs can provide insight into SOA mechanisms, care must be taken in deriving quantitative results from OFRs, which are often designed with slightly different geometries and operated under a variety of conditions. For example, recent OFR modeling results (Peng et al., 2019) demonstrated that the working conditions (e.g., light intensity and wavelength, humidity, and external OH reactivity) could influence the

RO_2 fate and result in less atmospherically relevant chemical mechanisms for SOA formation in the OFR.

Variability in the qualitative and/or mechanistic SOA information derived from OFRs is also possible. In particular, previous OFR studies (Lambe et al., 2012; Chen et al., 2013; Tkacik et al., 2014; Lambe et al., 2015; Ortega et al., 2016; Palm et al., 2016) have attributed large decreases in SOA yields at moderate to high photochemical age (typically after 4–5 equivalent days) to the dominant role of gas-phase fragmentation reactions. However, the current study indicates that the impact of fragmentation on SOA yields from various sources is minimal in the ECCC-OFR, likely due to reduced wall losses relative to other OFRs, whose fluid dynamics are not entirely laminar as suggested previously (Huang et al., 2017; Mitroo et al., 2018). Accounting for the fate of LVOCs (Palm et al., 2016) in the ECCC-OFR further indicates that the impact of fragmentation on SOA yields in the ambient atmosphere will be even smaller than that within the OFR. This implies that modeling SOA formation to include the impacts of fragmentation should be carefully evaluated, especially if using OFR data to provide empirical factors for fragmentation (Chen et al., 2013). However, the current data also indicate that the impact of fragmentation on SOA yields in OFRs can be significantly reduced through the use of seed particles, which increase the fraction of LVOCs which condense on aerosols ($F_{aerosol}$). This suggests that future laboratory OFR experiments studying SOA yields should be conducted with seed particles to obtain more relevant qualitative and quantitative data.

Application of the ECCC-OFR to OS-related precursor mixtures indicates that lower-volatility OS ore and bitumen vapors have significantly higher yields (maximum of ~ 0.6–0.7 for seeded experiments after LVOC-fate correction) than those from higher-volatility naphtha, dilbit, and tailings pond vapors (maximum of ~ 0.2–0.3 under the same conditions). The relatively high SOA yields from OS ore, together with the similar elemental ratios between ambient measurements and OFR experiments, are consistent with open-pit mining activities being the largest contributor to the observed SOA downwind of the OS operations (Liggio et al., 2016). The SOA yields and elemental ratio analysis also suggest that cyclic alkanes are import contributors to OS-related SOA. The OS SOA information derived here, for the range of precursor mixtures encountered in the oil sands, can be used to improve parameterizations of SOA for the OS region through source-specific inputs of SOA precursor properties and SOA yields and to evaluate the subsequent regional modeling of SOA (Stroud et al., 2018). The attribution of observed industrial SOA in the oil sands to specific sources (i.e., OS ore emissions from open-pit mining) supports the potential for future mitigation strategies for reducing SOA from this sector.

Author contributions. KL and JL designed the OFR and the experiments; KL conducted the experiments; PL and KL measured the volatility distributions; KL analyzed the data and wrote the paper, with contributions from JL; and PL, CH, QL, and SML commented on the paper.

References

Alboudwarej, H., Felix, J., Taylor, S., Badry, R., Bremner, C., Brough, B., Skeates, C., Baker, A., Palmer, D., Pattison, K., Beshry, M., Krawchuk, P., Brown, G., Calvo, R., Canas Triana, J. A., Hathcock, R., Koerner, K., Hughes, T., Kundu, D., de Cárdenas, J. L., and West, C.: Highlighting heavy oil, Oilfield Rev., 18, 34–53, 2006.

Atkinson, R. and Arey, J.: Atmospheric Degradation of Volatile Organic Compounds, Chem. Rev., 103, 4605–4638, https://doi.org/10.1021/cr0206420, 2003.

Bruns, E. A., El Haddad, I., Keller, A., Klein, F., Kumar, N. K., Pieber, S. M., Corbin, J. C., Slowik, J. G., Brune, W. H., Baltensperger, U., and Prévôt, A. S. H.: Inter-comparison of laboratory smog chamber and flow reactor systems on organic aerosol yield and composition, Atmos. Meas. Tech., 8, 2315–2332, https://doi.org/10.5194/amt-8-2315-2015, 2015.

Canagaratna, M. R., Jimenez, J. L., Kroll, J. H., Chen, Q., Kessler, S. H., Massoli, P., Hildebrandt Ruiz, L., Fortner, E., Williams, L. R., Wilson, K. R., Surratt, J. D., Donahue, N. M., Jayne, J. T., and Worsnop, D. R.: Elemental ratio measurements of organic compounds using aerosol mass spectrometry: characterization,

improved calibration, and implications, Atmos. Chem. Phys., 15, 253–272, https://doi.org/10.5194/acp-15-253-2015, 2015.

Chen, S., Brune, W. H., Lambe, A. T., Davidovits, P., and Onasch, T. B.: Modeling organic aerosol from the oxidation of α-pinene in a Potential Aerosol Mass (PAM) chamber, Atmos. Chem. Phys., 13, 5017–5031, https://doi.org/10.5194/acp-13-5017-2013, 2013.

Donahue, N. M., Robinson, A. L., Stanier, C. O., and Pandis, S. N.: Coupled partitioning, dilution, and chemical aging of semivolatile organics, Environ. Sci. Technol., 40, 2635–2643, https://doi.org/10.1021/es052297c, 2006.

Donahue, N. M., Kroll, J. H., Pandis, S. N., and Robinson, A. L.: A two-dimensional volatility basis set – Part 2: Diagnostics of organic-aerosol evolution, Atmos. Chem. Phys., 12, 615–634, https://doi.org/10.5194/acp-12-615-2012, 2012.

Eddingsaas, N. C., Loza, C. L., Yee, L. D., Chan, M., Schilling, K. A., Chhabra, P. S., Seinfeld, J. H., and Wennberg, P. O.: α-pinene photooxidation under controlled chemical conditions – Part 2: SOA yield and composition in low- and high-NO$_x$ environments, Atmos. Chem. Phys., 12, 7413–7427, https://doi.org/10.5194/acp-12-7413-2012, 2012.

Hallquist, M., Wenger, J. C., Baltensperger, U., Rudich, Y., Simpson, D., Claeys, M., Dommen, J., Donahue, N. M., George, C., Goldstein, A. H., Hamilton, J. F., Herrmann, H., Hoffmann, T., Iinuma, Y., Jang, M., Jenkin, M. E., Jimenez, J. L., Kiendler-Scharr, A., Maenhaut, W., McFiggans, G., Mentel, Th. F., Monod, A., Prévôt, A. S. H., Seinfeld, J. H., Surratt, J. D., Szmigielski, R., and Wildt, J.: The formation, properties and impact of secondary organic aerosol: current and emerging issues, Atmos. Chem. Phys., 9, 5155–5236, https://doi.org/10.5194/acp-9-5155-2009, 2009.

Han, Y., Stroud, C. A., Liggio, J., and Li, S.-M.: The effect of particle acidity on secondary organic aerosol formation from α-pinene photooxidation under atmospherically relevant conditions, Atmos. Chem. Phys., 16, 13929–13944, https://doi.org/10.5194/acp-16-13929-2016, 2016.

Harner, T., Rauert, C., Muir, D., Schuster, J. K., Hsu, Y.-M., Zhang, L., Marson, G., Watson, J. G., Ahad, J., Cho, S., Jariyasopit, N., Kirk, J., Korosi, J., Landis, M. S., Martin, J. W., Zhang, Y., Fernie, K., Wentworth, G. R., Wnorowski, A., Dabek, E., Charland, J.-P., Pauli, B., Wania, F., Galarneau, E., Cheng, I., Makar, P., Whaley, C., Chow, J. C., and Wang, X.: Air synthesis review: polycyclic aromatic compounds in the oil sands region, Environ. Rev., 26, 430–468, https://doi.org/10.1139/er-2018-0039, 2018.

Heald, C. L., Kroll, J. H., Jimenez, J. L., Docherty, K. S., DeCarlo, P. F., Aiken, A. C., Chen, Q., Martin, S. T., Farmer, D. K., and Artaxo, P.: A simplified description of the evolution of organic aerosol composition in the atmosphere, Geophys. Res. Lett., 37, L08803, https://doi.org/10.1029/2010gl042737, 2010.

Hildebrandt, L., Donahue, N. M., and Pandis, S. N.: High formation of secondary organic aerosol from the photo-oxidation of toluene, Atmos. Chem. Phys., 9, 2973–2986, https://doi.org/10.5194/acp-9-2973-2009, 2009.

Hofzumahaus, A., Rohrer, F., Lu, K., Bohn, B., Brauers, T., Chang, C.-C., Fuchs, H., Holland, F., Kita, K., Kondo, Y., Li, X., Lou, S., Shao, M., Zeng, L., Wahner, A., and Zhang, Y.: Amplified Trace Gas Removal in the Troposphere, Science, 324, 1702–1704, https://doi.org/10.1126/science.1164566, 2009.

Huang, Y., Coggon, M. M., Zhao, R., Lignell, H., Bauer, M. U., Flagan, R. C., and Seinfeld, J. H.: The Caltech Photooxidation Flow Tube reactor: design, fluid dynamics and characterization, Atmos. Meas. Tech., 10, 839–867, https://doi.org/10.5194/amt-10-839-2017, 2017.

Hunter, J. F., Carrasquillo, A. J., Daumit, K. E., and Kroll, J. H.: Secondary organic aerosol formation from acyclic, monocyclic, and polycyclic alkanes, Environ. Sci. Technol., 48, 10227–10234, https://doi.org/10.1021/es502674s, 2014.

Ihalainen, M., Tiitta, P., Czech, H., Yli-Pirilä, P., Hartikainen, A., Kortelainen, M., Tissari, J., Stengel, B., Sklorz, M., Suhonen, H., Lamberg, H., Leskinen, A., Kiendler-Scharr, A., Harndorf, H., Zimmermann, R., Jokiniemi, J., and Sippula, O.: A novel high-volume Photochemical Emission Aging flow tube Reactor (PEAR), Aerosol Sci. Tech., 53, 276–294, https://doi.org/10.1080/02786826.2018.1559918, 2019.

Jathar, S. H., Friedman, B., Galang, A. A., Link, M. F., Brophy, P., Volckens, J., Eluri, S., and Farmer, D. K.: Linking Load, Fuel, and Emission Controls to Photochemical Production of Secondary Organic Aerosol from a Diesel Engine, Environ. Sci. Technol., 51, 1377–1386, https://doi.org/10.1021/acs.est.6b04602, 2017.

Jimenez, J. L., Canagaratna, M. R., Donahue, N. M., Prevot, A. S., Zhang, Q., Kroll, J. H., DeCarlo, P. F., Allan, J. D., Coe, H., Ng, N. L., Aiken, A. C., Docherty, K. S., Ulbrich, I. M., Grieshop, A. P., Robinson, A. L., Duplissy, J., Smith, J. D., Wilson, K. R., Lanz, V. A., Hueglin, C., Sun, Y. L., Tian, J., Laaksonen, A., Raatikainen, T., Rautiainen, J., Vaattovaara, P., Ehn, M., Kulmala, M., Tomlinson, J. M., Collins, D. R., Cubison, M. J., Dunlea, E. J., Huffman, J. A., Onasch, T. B., Alfarra, M. R., Williams, P. I., Bower, K., Kondo, Y., Schneider, J., Drewnick, F., Borrmann, S., Weimer, S., Demerjian, K., Salcedo, D., Cottrell, L., Griffin, R., Takami, A., Miyoshi, T., Hatakeyama, S., Shimono, A., Sun, J. Y., Zhang, Y. M., Dzepina, K., Kimmel, J. R., Sueper, D., Jayne, J. T., Herndon, S. C., Trimborn, A. M., Williams, L. R., Wood, E. C., Middlebrook, A. M., Kolb, C. E., Baltensperger, U., and Worsnop, D. R.: Evolution of organic aerosols in the atmosphere, Science, 326, 1525–1529, https://doi.org/10.1126/science.1180353, 2009.

Jung, K., Ok, Y. S., and Chang, S. X.: Sulfate adsorption properties of acid-sensitive soils in the Athabasca oil sands region in Alberta, Canada, Chemosphere, 84, 457–463, https://doi.org/10.1016/j.chemosphere.2011.03.034, 2011.

Kang, E., Root, M. J., Toohey, D. W., and Brune, W. H.: Introducing the concept of Potential Aerosol Mass (PAM), Atmos. Chem. Phys., 7, 5727–5744, https://doi.org/10.5194/acp-7-5727-2007, 2007.

Kang, E., Toohey, D. W., and Brune, W. H.: Dependence of SOA oxidation on organic aerosol mass concentration and OH exposure: experimental PAM chamber studies, Atmos. Chem. Phys., 11, 1837–1852, https://doi.org/10.5194/acp-11-1837-2011, 2011.

Karjalainen, P., Timonen, H., Saukko, E., Kuuluvainen, H., Saarikoski, S., Aakko-Saksa, P., Murtonen, T., Bloss, M., Dal Maso, M., Simonen, P., Ahlberg, E., Svenningsson, B., Brune, W. H., Hillamo, R., Keskinen, J., and Rönkkö, T.: Time-resolved characterization of primary particle emissions and secondary particle formation from a modern gasoline passenger car, Atmos. Chem. Phys., 16, 8559–8570, https://doi.org/10.5194/acp-16-8559-2016, 2016.

Kirk, J. L., Muir, D. C., Gleason, A., Wang, X., Lawson, G., Frank, R. A., Lehnherr, I., and Wrona, F.: Atmospheric deposition of mercury and methylmercury to landscapes and waterbodies of the Athabasca oil sands region, Environ. Sci. Technol., 48, 7374–7383, https://doi.org/10.1021/es500986r, 2014.

Kroll, J. H. and Seinfeld, J. H.: Chemistry of secondary organic aerosol: Formation and evolution of low-volatility organics in the atmosphere, Atmos. Environ., 42, 3593–3624, https://doi.org/10.1016/j.atmosenv.2008.01.003, 2008.

Kroll, J. H., Chan, A. W. H., Ng, N. L., Flagan, R. C., and Seinfeld, J. H.: Reactions of semivolatile organics and their effects on secondary organic aerosol formation, Environ. Sci. Technol., 41, 3545–3550, https://doi.org/10.1021/es062059x, 2007.

Kroll, J. H., Smith, J. D., Che, D. L., Kessler, S. H., Worsnop, D. R., and Wilson, K. R.: Measurement of fragmentation and functionalization pathways in the heterogeneous oxidation of oxidized organic aerosol, Phys. Chem. Chem. Phys., 11, 8005–8014, https://doi.org/10.1039/b905289e, 2009.

Lambe, A., Massoli, P., Zhang, X., Canagaratna, M., Nowak, J., Daube, C., Yan, C., Nie, W., Onasch, T., Jayne, J., Kolb, C., Davidovits, P., Worsnop, D., and Brune, W.: Controlled nitric oxide production via $O(^1D) + N_2O$ reactions for use in oxidation flow reactor studies, Atmos. Meas. Tech., 10, 2283-2298, https://doi.org/10.5194/amt-10-2283-2017, 2017.

Lambe, A. T., Ahern, A. T., Williams, L. R., Slowik, J. G., Wong, J. P. S., Abbatt, J. P. D., Brune, W. H., Ng, N. L., Wright, J. P., Croasdale, D. R., Worsnop, D. R., Davidovits, P., and Onasch, T. B.: Characterization of aerosol photooxidation flow reactors: heterogeneous oxidation, secondary organic aerosol formation and cloud condensation nuclei activity measurements, Atmos. Meas. Tech., 4, 445–461, https://doi.org/10.5194/amt-4-445-2011, 2011.

Lambe, A. T., Onasch, T. B., Croasdale, D. R., Wright, J. P., Martin, A. T., Franklin, J. P., Massoli, P., Kroll, J. H., Canagaratna, M. R., Brune, W. H., Worsnop, D. R., and Davidovits, P.: Transitions from functionalization to fragmentation reactions of laboratory secondary organic aerosol (SOA) generated from the OH oxidation of alkane precursors, Environ. Sci. Technol., 46, 5430–5437, https://doi.org/10.1021/es300274t, 2012.

Lambe, A. T., Chhabra, P. S., Onasch, T. B., Brune, W. H., Hunter, J. F., Kroll, J. H., Cummings, M. J., Brogan, J. F., Parmar, Y., Worsnop, D. R., Kolb, C. E., and Davidovits, P.: Effect of oxidant concentration, exposure time, and seed particles on secondary organic aerosol chemical composition and yield, Atmos. Chem. Phys., 15, 3063–3075, https://doi.org/10.5194/acp-15-3063-2015, 2015.

Li, K., Li, J., Wang, W., Li, J., Peng, C., Wang, D., and Ge, M.: Effects of Gas-Particle Partitioning on Refractive Index and Chemical Composition of m-Xylene Secondary Organic Aerosol, J. Phys. Chem. A, 122, 3250–3260, https://doi.org/10.1021/acs.jpca.7b12792, 2018.

Li, R., Palm, B. B., Ortega, A. M., Hlywiak, J., Hu, W., Peng, Z., Day, D. A., Knote, C., Brune, W. H., de Gouw, J. A., and Jimenez, J. L.: Modeling the radical chemistry in an oxidation flow reactor: radical formation and recycling, sensitivities, and the OH exposure estimation equation, J. Phys. Chem. A, 119, 4418–4432, https://doi.org/10.1021/jp509534k, 2015.

Li, S.-M., Leithead, A., Moussa, S. G., Liggio, J., Moran, M. D., Wang, D., Hayden, K., Darlington, A., Gordon, M., Staebler, R.,

Makar, P. A., Stroud, C. A., McLaren, R., Liu, P. S. K., O'Brien, J., Mittermeier, R. L., Zhang, J., Marson, G., Cober, S. G., Wolde, M., and Wentzell, J. J. B.: Differences between measured and reported volatile organic compound emissions from oil sands facilities in Alberta, Canada, P. Natl. Acad. Sci. USA, 114, E3756-E3765, https://doi.org/10.1073/pnas.1617862114, 2017.

Liggio, J., Li, S. M., Hayden, K., Taha, Y. M., Stroud, C., Darlington, A., Drollette, B. D., Gordon, M., Lee, P., Liu, P., Leithead, A., Moussa, S. G., Wang, D., O'Brien, J., Mittermeier, R. L., Brook, J. R., Lu, G., Staebler, R. M., Han, Y., Tokarek, T. W., Osthoff, H. D., Makar, P. A., Zhang, J., Plata, D. L., and Gentner, D. R.: Oil sands operations as a large source of secondary organic aerosols, Nature, 534, 91–94, https://doi.org/10.1038/nature17646, 2016.

Lim, Y. B. and Ziemann, P. J.: Products and mechanism of secondary organic aerosol formation from reactions of n-alkanes with OH radicals in the presence of NO_x, Environ. Sci. Technol., 39, 9229–9236, https://doi.org/10.1021/es051447g, 2005.

Lim, Y. B. and Ziemann, P. J.: Effects of Molecular Structure on Aerosol Yields from OH Radical-Initiated Reactions of Linear, Branched, and Cyclic Alkanes in the Presence of NO_x, Environ. Sci. Technol., 43, 2328–2334, https://doi.org/10.1021/es803389s, 2009.

Liu, Y., Liggio, J., Harner, T., Jantunen, L., Shoeib, M., and Li, S. M.: Heterogeneous OH initiated oxidation: a possible explanation for the persistence of organophosphate flame retardants in air, Environ. Sci. Technol., 48, 1041–1048, https://doi.org/10.1021/es404515k, 2014.

Loza, C. L., Craven, J. S., Yee, L. D., Coggon, M. M., Schwantes, R. H., Shiraiwa, M., Zhang, X., Schilling, K. A., Ng, N. L., Canagaratna, M. R., Ziemann, P. J., Flagan, R. C., and Seinfeld, J. H.: Secondary organic aerosol yields of 12-carbon alkanes, Atmos. Chem. Phys., 14, 1423–1439, https://doi.org/10.5194/acp-14-1423-2014, 2014.

Makar, P. A., Akingunola, A., Aherne, J., Cole, A. S., Aklilu, Y.-A., Zhang, J., Wong, I., Hayden, K., Li, S.-M., Kirk, J., Scott, K., Moran, M. D., Robichaud, A., Cathcart, H., Baratzedah, P., Pabla, B., Cheung, P., Zheng, Q., and Jeffries, D. S.: Estimates of exceedances of critical loads for acidifying deposition in Alberta and Saskatchewan, Atmos. Chem. Phys., 18, 9897–9927, https://doi.org/10.5194/acp-18-9897-2018, 2018.

Mao, J., Ren, X., Brune, W. H., Olson, J. R., Crawford, J. H., Fried, A., Huey, L. G., Cohen, R. C., Heikes, B., Singh, H. B., Blake, D. R., Sachse, G. W., Diskin, G. S., Hall, S. R., and Shetter, R. E.: Airborne measurement of OH reactivity during INTEX-B, Atmos. Chem. Phys., 9, 163–173, https://doi.org/10.5194/acp-9-163-2009, 2009.

Mitroo, D., Sun, Y., Combest, D. P., Kumar, P., and Williams, B. J.: Assessing the degree of plug flow in oxidation flow reactors (OFRs): a study on a potential aerosol mass (PAM) reactor, Atmos. Meas. Tech., 11, 1741–1756, https://doi.org/10.5194/amt-11-1741-2018, 2018.

Mohr, S. H. and Evans, G. M.: Long term prediction of unconventional oil production, Energ. Policy, 38, 265–276, https://doi.org/10.1016/j.enpol.2009.09.015, 2010.

Ng, N. L., Chhabra, P. S., Chan, A. W. H., Surratt, J. D., Kroll, J. H., Kwan, A. J., McCabe, D. C., Wennberg, P. O., Sorooshian, A., Murphy, S. M., Dalleska, N. F., Flagan, R. C., and Seinfeld, J. H.: Effect of NO_x level on secondary organic aerosol (SOA) forma-

tion from the photooxidation of terpenes, Atmos. Chem. Phys., 7, 5159–5174, https://doi.org/10.5194/acp-7-5159-2007, 2007.

Ng, N. L., Canagaratna, M. R., Jimenez, J. L., Chhabra, P. S., Seinfeld, J. H., and Worsnop, D. R.: Changes in organic aerosol composition with aging inferred from aerosol mass spectra, Atmos. Chem. Phys., 11, 6465–6474, https://doi.org/10.5194/acp-11-6465-2011, 2011.

Odum, J. R., Hoffmann, T., Bowman, F., Collins, D., Flagan, R. C., and Seinfeld, J. H.: Gas/particle partitioning and secondary organic aerosol yields, Environ. Sci. Technol., 30, 2580–2585, https://doi.org/10.1021/es950943+, 1996.

Ortega, A. M., Day, D. A., Cubison, M. J., Brune, W. H., Bon, D., de Gouw, J. A., and Jimenez, J. L.: Secondary organic aerosol formation and primary organic aerosol oxidation from biomass-burning smoke in a flow reactor during FLAME-3, Atmos. Chem. Phys., 13, 11551–11571, https://doi.org/10.5194/acp-13-11551-2013, 2013.

Ortega, A. M., Hayes, P. L., Peng, Z., Palm, B. B., Hu, W., Day, D. A., Li, R., Cubison, M. J., Brune, W. H., Graus, M., Warneke, C., Gilman, J. B., Kuster, W. C., de Gouw, J., Gutiérrez-Montes, C., and Jimenez, J. L.: Real-time measurements of secondary organic aerosol formation and aging from ambient air in an oxidation flow reactor in the Los Angeles area, Atmos. Chem. Phys., 16, 7411–7433, https://doi.org/10.5194/acp-16-7411-2016, 2016.

Owen, N. A., Inderwildi, O. R., and King, D. A.: The status of conventional world oil reserves – Hype or cause for concern?, Energ. Policy, 38, 4743–4749, https://doi.org/10.1016/j.enpol.2010.02.026, 2010.

Palm, B. B., Campuzano-Jost, P., Ortega, A. M., Day, D. A., Kaser, L., Jud, W., Karl, T., Hansel, A., Hunter, J. F., Cross, E. S., Kroll, J. H., Peng, Z., Brune, W. H., and Jimenez, J. L.: In situ secondary organic aerosol formation from ambient pine forest air using an oxidation flow reactor, Atmos. Chem. Phys., 16, 2943–2970, https://doi.org/10.5194/acp-16-2943-2016, 2016.

Peng, Z., Palm, B. B., Day, D. A., Talukdar, R. K., Hu, W., Lambe, A. T., Brune, W. H., and Jimenez, J. L.: Model Evaluation of New Techniques for Maintaining High-NO Conditions in Oxidation Flow Reactors for the Study of OH-Initiated Atmospheric Chemistry, ACS Earth and Space Chemistry, 2, 72–86, https://doi.org/10.1021/acsearthspacechem.7b00070, 2018.

Peng, Z., Lee-Taylor, J., Orlando, J. J., Tyndall, G. S., and Jimenez, J. L.: Organic peroxy radical chemistry in oxidation flow reactors and environmental chambers and their atmospheric relevance, Atmos. Chem. Phys., 19, 813–834, https://doi.org/10.5194/acp-19-813-2019, 2019.

Simonen, P., Saukko, E., Karjalainen, P., Timonen, H., Bloss, M., Aakko-Saksa, P., Rönkkö, T., Keskinen, J., and Dal Maso, M.: A new oxidation flow reactor for measuring secondary aerosol formation of rapidly changing emission sources, Atmos. Meas. Tech., 10, 1519–1537, https://doi.org/10.5194/amt-10-1519-2017, 2017.

Simpson, I. J., Blake, N. J., Barletta, B., Diskin, G. S., Fuelberg, H. E., Gorham, K., Huey, L. G., Meinardi, S., Rowland, F. S., Vay, S. A., Weinheimer, A. J., Yang, M., and Blake, D. R.: Characterization of trace gases measured over Alberta oil sands mining operations: 76 speciated C2–C10 volatile organic compounds (VOCs), CO_2, CH_4, CO, NO, NO_2, NO_y, O_3 and SO_2, Atmos.

Chem. Phys., 10, 11931–11954, https://doi.org/10.5194/acp-10-11931-2010, 2010.

Stone, D., Whalley, L. K., and Heard, D. E.: Tropospheric OH and HO_2 radicals: field measurements and model comparisons, Chem. Soc. Rev., 41, 6348–6404, https://doi.org/10.1039/C2CS35140D, 2012.

Stroud, C. A., Makar, P. A., Zhang, J., Moran, M. D., Akingunola, A., Li, S.-M., Leithead, A., Hayden, K., and Siu, M.: Improving air quality model predictions of organic species using measurement-derived organic gaseous and particle emissions in a petrochemical-dominated region, Atmos. Chem. Phys., 18, 13531–13545, https://doi.org/10.5194/acp-18-13531-2018, 2018.

Tkacik, D. S., Presto, A. A., Donahue, N. M., and Robinson, A. L.: Secondary organic aerosol formation from intermediate-volatility organic compounds: cyclic, linear, and branched alkanes, Environ. Sci. Technol., 46, 8773–8781, https://doi.org/10.1021/es301112c, 2012.

Tkacik, D. S., Lambe, A. T., Jathar, S., Li, X., Presto, A. A., Zhao, Y., Blake, D., Meinardi, S., Jayne, J. T., Croteau, P. L., and Robinson, A. L.: Secondary organic aerosol formation from in-use motor vehicle emissions using a potential aerosol mass reactor, Environ. Sci. Technol., 48, 11235–11242, https://doi.org/10.1021/es502239v, 2014.

Tokarek, T. W., Odame-Ankrah, C. A., Huo, J. A., McLaren, R., Lee, A. K. Y., Adam, M. G., Willis, M. D., Abbatt, J. P. D., Mihele, C., Darlington, A., Mittermeier, R. L., Strawbridge, K., Hayden, K. L., Olfert, J. S., Schnitzler, E. G., Brownsey, D. K., Assad, F. V., Wentworth, G. R., Tevlin, A. G., Worthy, D. E. J., Li, S.-M., Liggio, J., Brook, J. R., and Osthoff, H. D.: Principal component analysis of summertime ground site measurements in the Athabasca oil sands with a focus on analytically unresolved intermediate-volatility organic compounds, Atmos. Chem. Phys., 18, 17819–17841, https://doi.org/10.5194/acp-18-17819-2018, 2018.

Veres, P., Gilman, J. B., Roberts, J. M., Kuster, W. C., Warneke, C., Burling, I. R., and de Gouw, J.: Development and validation of a portable gas phase standard generation and calibration system for volatile organic compounds, Atmos. Meas. Tech., 3, 683–691, https://doi.org/10.5194/amt-3-683-2010, 2010.

Zhang, X., Cappa, C. D., Jathar, S. H., McVay, R. C., Ensberg, J. J., Kleeman, M. J., and Seinfeld, J. H.: Influence of vapor wall loss in laboratory chambers on yields of secondary organic aerosol, P. Natl. Acad. Sci. USA, 111, 5802–5807, 2014.